Astronomy & Astrophysics manuscript no.
(will be inserted by hand later)

Radio observations of new galactic bulge planetary nebulae

G.C. Van de Steene[1,3] and G.H. Jacoby[2,4] ⋆

[1] Royal Observatory of Belgium, Ringlaan 3, 1180 Brussels, Belgium
[2] National Optical Astronomical Observatories, P.O. Box 26732, Tucson, AZ 85726, U.S.A.
[3] Research School for Astronomy and Astrophysics, Private Bag P.O., Weston Creek, ACT 2611, Australia
[4] WIYN Observatory, P.O. Box 26732, Tucson, AZ 85726, U.S.A.

received / accepted

Abstract. We observed 64 newly identified galactic bulge planetary nebulae in the radio continuum at 3 and 6 cm with the Australia Telescope Compact Array. We present their radio images, positions, flux densities, and angular sizes. The survey appears to have detected a larger ratio of more extended planetary nebulae with low surface brightness than in previous surveys. We calculated their distances according to Van de Steene & Zijlstra (1995). We find that most of the new sample is located on the near side around the galactic center and closer in than the previously known bulge PNe. Based on Hα images and spectroscopic data, we calculated the total Hα flux. We compare this flux value with the radio flux density and derive the extinction. We confirm that the distribution of the extinction values around the galactic center rises toward the center, as expected.

Key words. planetary nebulae: general, galactic bulge, radio

1. Introduction

Planetary Nebulae (PNe) are bright emission line objects, observable throughout the Galaxy. They are excellent probes of abundance gradients, the chemical enrichment history of the interstellar medium, the effects of metallicity on stellar evolution, and kinematics.

Most small PNe (∼90%) within 10° of the galactic center are physically close to it (Pottasch & Acker 1989). Since they can be assumed to be at the same known distance of ∼7.8 kpc, their distance-dependent parameters, such as luminosity and size, can be determined. These parameters are needed to define the underlying population. The chemical composition and the central star parameters are computed via self-consistent photo-ionization modelling of the nebula. Because luminosity correlates with the central star mass, which correlates with the progenitor mass, which, in turn, correlates with stellar age, the relationship between age and composition can be deduced (Dopita et al. 1997, Walsh et al. 2000). The chemical enrichment history of the Bulge could be tracked using PNe.

We surveyed a 4 x 4 degree field centered on the galactic center in [S III]λ9532 and a continuum band at KPNO with the 60-cm Schmidt telescope and a 2048 x 2048 pixels thick STIS CCD in July 1994 and June 1995. The field of view was 65′ x 65′ and the pixel size 2″. This survey has uncovered 95 new PN candidates in addition to the 34 previously known in this region (Acker et al. 1992, Kohoutek 1994). 45 PNe were confirmed via optical spectroscopy with the 1.52-m ESO telescope and the Boller & Chivens spectrograph, while 19 fainter ones were confirmed at the CTIO 4-m with the RC spectrograph (Van de Steene & Jacoby 2001, in preparation).

Accurate radio flux densities and angular diameters are crucial to obtain a good photo-ionization model of the PNe (van Hoof & Van de Steene 1999). The very high extinction causes the Hβ line to be faint or even undetected in the optical spectra. Hence the radio flux density is needed to determine the extinction and the total ionizing flux.

In this article we present the radio continuum observations of 64 PNe confirmed spectroscopically with the ESO 1.52-m and CTIO 4-m telescopes. We describe the observations in Sect. 2 and the data reduction in Sect. 3. The results are presented in Sect. 4. The improved method for determining the distances, based on a relationship between radii and radio surface brightness (Van de Steene & Zijlstra 1995) is used in Sect. 5 to determine the distances of the PNe and discuss their distribution in

Send offprint requests to: G.C. Van de Steene[1],e-mail: gsteene@oma.be

⋆ Based on data acquired at the Australia Telescope Compact Array. The Australia Telescope is funded by the Commonwealth of Australia for operation as a National Facility managed by CSIRO.

the galactic bulge. In Sect. 6 we determine the extinction values of these new bulge PNe.

2. Observations

Radio continuum observations for 64 new PNe which had been confirmed spectroscopically at the ESO 1.52-m and CTIO 4-m telescopes were obtained with the Australia Telescope Compact Array. The array was in configuration # 6A. The shortest baseline was 337 m and the longest 5939 m. The bandwidth was 128 MHz centered at 4800 MHz and 8640 MHz, corresponding to 6 and 3 cm respectively. The synthesized beam for the 6 km array at 6 cm is $\sim 2''$ and $\sim 1''$ at 3 cm. According to the ACA manual, the largest well imaged structure in a 60 min observation is $30''$ at 6 cm and $15''$ at 3 cm. Consequently we expected all our sources to be well imaged at 6 cm and virtually all at 3 cm. Forty PNe were observed at 3 and 6 cm simultaneously for 12 h on each of 12, 13, 16 & 17 February 1997 and 36 PNe were observed during 10 h on each of 24, 25, and 26 May 1999. In 1997 each subsample contained 10 PNe and each PN was observed for 5 min every hour. In 1999 each subsample contained 6 PNe and each PN was observed for 8 min every hour. The total quality integration time per PN was at least 50 min in 1997 and 80 min in 1999. To avoid artifacts at the center of the field we offsetted the positions $30''$ in declination. At the beginning and the end of each 12 h shift the primary flux density calibrator 1934-638 was observed for 5 to 10 min. The phase calibrator VLA 1730-130 and VLA 1748-253 were observed about every 20 min for 2 min.

3. Data Reduction

The data were reduced using the package `Miriad` following standard reduction steps as described in the reference guide by Bob Sault and Neil Killeen (Sault et al. 1995) . The data were loaded, bad points flagged, and then split into single source files. The bandpass function and the antenna gains were determined as a function of time to calibrate the data. From the visibilities images were made using the multi-frequency synthesis technique and robust weighting with a robustness parameter of 0.5, which gives nearly the same sensitivity as natural weighting but with a significantly better beam. First a low resolution image of the primary beam was made to identify confusing sources. Next a high resolution image was made including all sources. These maps were `CLEAN`ed. Because we had offsetted the PNe from the field center, we applied the primary beam correction which amounted to about 1% at 6 cm and 2% at 3 cm. Self-calibration was not applied because the flux values of the PNe are too low. Contour plots of the detected PNe are presented in the Appendix.

4. Analysis and Results

4.1. Positions

In Table 1 we list the position of the peak flux density per beam of the PN at 6 cm together with the optical positions as determined from the Hα or [S III]λ9532 images (Jacoby & Van de Steene, 2001, in preparation). The peak of the radio emission is adopted as the PN position. If the PN is extended in the radio, the radio position may be off center. The radio position will be better determined for higher peak flux values and smaller PNe. It is also for this reason that we chose to use the value at 6 cm and not at 3 cm, where the resolution is twice as high and the signal to noise per beam lower for extended sources.

We note that the radio positions have a tendency to be offset towards the west of the optical position. In declination there is no clear tendency noticeable in the offsets.

The optical and radio positions agree very well. PNe for which the radio position differs more than 2 $''$ in RA or DEC from the optical position are extended and the peak in the radio is usually not centered.

Of the 64 PNe observed, 7 were not detected: JaSt 7, 21, 45, 80, 88, 92, and 96. Most likely they are very extended and have a surface brightness that is too low to be detected in the radio. They are also very faint in the Hα images and their Hα flux values are very uncertain (Jacoby & Van de Steene 2001, in preparation). All but JaSt 96 were also faint and extended in the [S III]λ9532 images.

4.2. Radio flux densities

Table 2 gives the radio flux densities at 6 and 3 cm.

If a Gaussian model provided a satisfactory fit to the surface brightness the total Gaussian flux density was adopted. This was mostly the case for small, unresolved PNe. If the PN was extended the intensities within the 2 or 3 σ level contour were summed. This value was compared with the statistics over a larger region across the nebula to obtain an error estimate (Fomalont, 1989).

For JaSt 69 only a small 3 σ blob at the right position indicated the presence of a PN. No flux or size values could be determined. In some cases several blobs indicated the presence of a PN at 3 cm and hence their flux is a lower limit. Some objects detected at 6 cm, but having low peak flux density per beam, could not be seen at 3 cm.

PNe are normally optically thin at 6 cm in which case its 3 cm flux density is about 95% of the 6 cm flux density. In our case this means that the flux densities are similar within the error-bars. However when a PN is already well resolved at 6 cm, more flux may have been missed at 3 cm where the beam is half the size, especially if the nebula is extended and of low surface brightness. It is clear that due to these factors the flux density at 3 cm is generally less well-determined than at 6 cm, except for the bright and compact PNe. When a PN is optically thick at 6 cm, its 3 cm flux density is expected to be three times the flux

Fig. 1. Histogram of the 6 cm flux values of previously known galactic bulge PNe with radio data and the new galactic bulge PNe (striped)

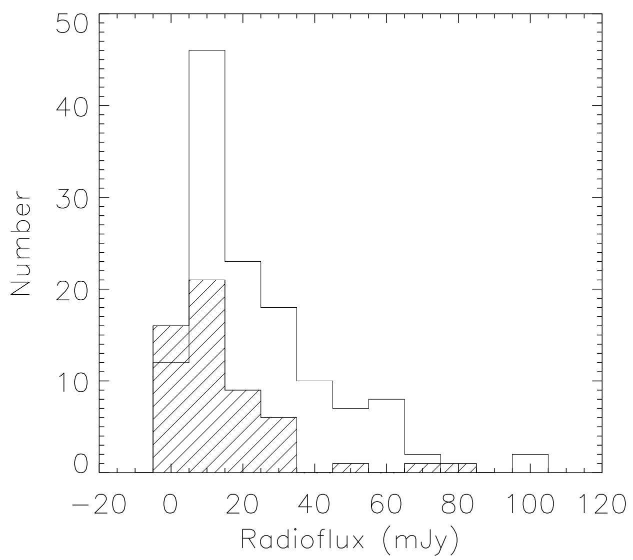

density at 6 cm. There are some PNe like JaSt 65 and JaSt 79 for which the 3 cm flux density is clearly higher than the 6 cm flux density and which are point sources. In this case the PNe may not yet be completely optically thin at 6 cm and should be quite young.

In Fig. 1 we plotted the histogram of the radio flux of the known and new galactic bulge PNe. We selected a sample of known galactic bulge PNe for which radio flux densities and angular diameters are available, as in Van de Steene & Zijlstra (1995). The new bulge PNe are within 2 degrees of the galactic center. None has a radio flux larger than 100 mJy and their angular sizes are smaller than $20''$. Hence they fulfill the same selection criteria as these previously known bulge PNe.

There is a larger number of PNe with low flux densities among the new bulge PNe than among the known ones. 67 % of the new PNe have a radio flux less than 15 mJy, while this is only 45 % for the known ones. Of the 7 known ones within 2 degrees of the galactic center only 2 have a radio flux below 15 mJy. The median flux for the new PNe is 11.3 mJy, while the median for the known bulge PNe is 17.0 mJy. Our rms noise level in the maps is similar to the 1 σ noise of 0.1 mJy in the 6 cm maps of Zijlstra et al. (1989). Apparently these faint and small PNe have just been missed in optical surveys done to date.

4.3. Angular Size

Table 2 also gives the angular size of the detected PNe. We chose to determine the angular size at 6 cm because at this wavelength the resolution was lower and thus gives the best signal to noise ratio for the extended nebulae. The diameter at 3 cm is given if it is better determined than at 6 cm, such as for very small and bright PNe.

Diameters may differ considerably depending upon how they are calculated. The diameter was derived by one of several ways depending on the structure of the brightness distribution. If a two-dimensional Gaussian fit provided a satisfactory model to the observed structureless surface distribution, its deconvolved FWHM major and minor axis are given. The equivalent diameter is the square root of their product. To obtain the full diameter, this value must be multiplied with a conversion factor which is a function of the beam FWHM and depends upon the intrinsic surface distribution of the source. We assumed a spherical constant emissivity shell of 0.5 and used formula 5 and Table 1 from van Hoof (2000) to estimate the true radii. For small objects, if the Gaussian deconvolution was well determined and similar at 3 and 6 cm, the FWHM at 3 cm is given. If the deconvolution produced a point source at 6 cm, the source size at 3 cm is given. If the source was still a point source at 3 cm, the beam-size is an upper limit. If the source was extended, a Gaussian model was usually not a good representation of the radio source. The diameter of the PN was measured on the contour at 50 % of the peak and deconvolved with the beam size. To determine the full diameter we determined the ratio of the flux density within the 3 σ contour with the flux density within the 50 % contour. Hence, we assumed that the flux decreased linearly with radius outside the 50 % contour. We checked that this procedure seemed to give very good agreement with the size measured based on the 3 σ contour. We didn't use the contour level at 10% of the peak (Zijlstra et al. 1989, Aaquist & Kwok 1990), because this was often below noise level.

It was noticed in the review paper by Pottasch (1992) that there is a selection against discovering both large and small PNe in the galactic bulge. 36 % of the new PNe have a diameter smaller than $5''$, while this is 71 % for the known ones. The median is $6\overset{''}{.}6$ for the new PNe and only $3\overset{''}{.}2$ for the known bulge PNe with radio data. We seem to identify relatively more larger PNe than in previous surveys. In regions with large extinction the [SIII]λ9532 line appears efficient in picking out the larger, low surface brightness PNe, and not only the small and dusty ones. Obviously these are the PNe which may have been missed in optical surveys.

5. Distances

Based on the flux densities and the angular equivalent diameters we calculated the statistical distances to the PNe as established in Van de Steene & Zijlstra (1995). The relation is not strictly valid for optically thick and very small nebulae which may have their distance overestimated. The distances will tend to be overestimated for PNe with lower surface brightness than average, while PNe with a higher surface brightness than average will tend to have their dis-

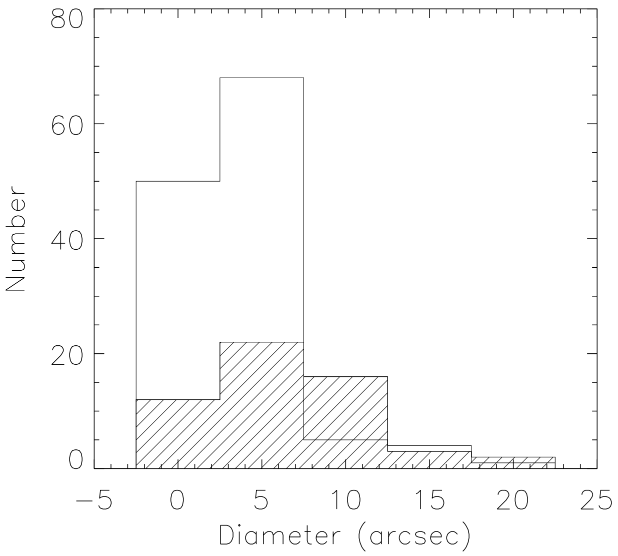

Fig. 2. Histogram of the size of the known galactic bulge PNe with radio data and the new galactic bulge PNe (striped)

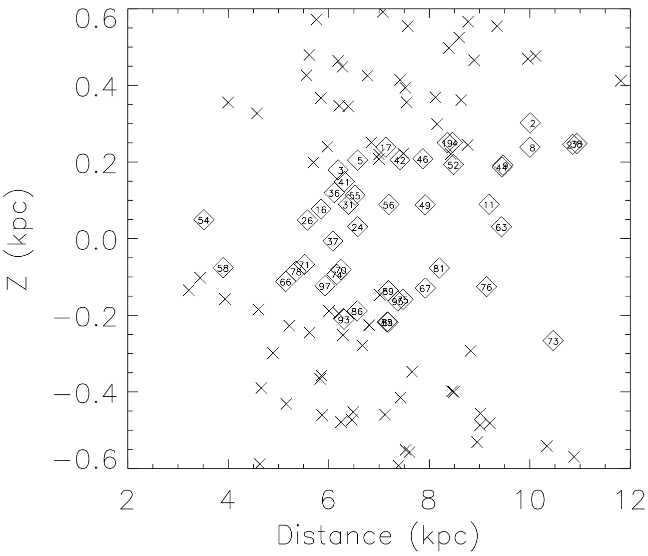

Fig. 4. Plot of the scale-height versus distance of the new galactic bulge PNe (diamonds) and the known galactic bulge PNe with radio data (crosses)

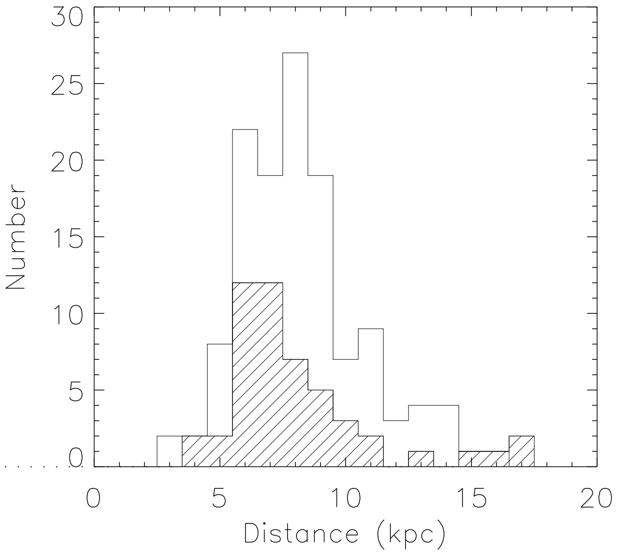

Fig. 3. Histogram showing the distribution of the distances of the new galactic bulge PNe (striped) and the known bulge PNe with radio data.

tances underestimated. However, statistically the distance distribution will be representative.

The distances are presented in Table 3. A histogram of the distance distribution is presented in Fig. 3. The median distance is 7.2 kpc, about 8% closer than the galactic center; presumably, the more distant PNe suffer greater extinction and fell below our detection limit in our survey.

In Fig. 4 we plotted the scale height versus the distance. It seems that we observe PNe at the edge of the galactic bulge. As we look further inward, the extinction probably becomes too large. The PNe further away are at larger scale height where, apparently, the extinction is less. The known PNe are generally further away from the galactic center, surrounding our new PNe. The median absolute scale height is 136 pc.

6. Extinction

We calculated the extinction E(B-V) comparing the radio flux densities with the total Hα flux values, which were obtained from images obtained with the NOAO 8k x 8k Mosaic Imager on the 0.9-m telescope at KPNO (Jacoby & Van de Steene 2001, in preparation). The flux values were corrected for the contribution of [N II]λ6548 & λ6584 based on spectra obtained at ESO and CTIO (Van de Steene & Jacoby, 2001, in preparation). The Hβ flux and radio flux density have the same dependency on electron density and the expected ratio is only a weak function of the electron temperature and helium abundance (Pottasch, 1984). The radio flux density and Hβ flux can be used to determine the extinction $c_{H\beta}$ = 1.46 E(B-V). Assuming the standard ratio of Hα / Hβ = 2.85, we used the Hα flux to predict the extinction: $c_{H\alpha}$ = E(B-V). The values of E(B-V) are presented in Table 3. All but one PN

Table 3. In this table we present the statistical distance in column 2, the scale height, radius, and ionized mass calculated using this distance in columns 3, 4, and 5 respectively, and E(B-V) = c_{H_β} / 1.46 in column 6. If the object was not detected in Hα, E(B-V) is marked with X. If no Hα image was obtained E(B-V) is marked with Z. In this case the E(B-V) value was derived from its spectrum. Uncertain values, due to uncertain radio flux or Hα flux values, are marked with a colon. PS stands for Point Source.

JaSt	Dist kpc	z pc	R pc	M_{ion} $M_{\odot}$	E(B-V)	Comment
1	14.6:	401.6:	0.20:	0.25:	2.5:	
2	10.0	305.7	0.15	0.19	2.0	
3	6.2	183.0	0.14	0.17	2.3	
4	8.5	258.9	0.23	0.29	1.9	
5	6.6	210.4	0.13	0.17	2.3	
8	10.0	241.9	0.17	0.22	2.1	
9	9.5	194.9	0.19	0.23	2.9	
11	9.2	91.6	0.24	0.31	3.7	
16	5.9	77.6	0.07	0.08	3.5	
17	7.1	242.5	0.14	0.17	1.8	
19	8.4	264.7	0.14	0.17	1.8	
23					2.4	PS
24	6.6	31.4	0.09	0.11	X	
26	5.6	49.7	0.15	0.19	X	
27	10.8	246.2	0.23	0.29	2.3	
31	6.4	91.2	0.14	0.17	3.7	
34	13.2	392.9	0.23	0.29	2.1	
36	6.1	120.2	0.05	0.06	2.7	
37	6.1	-6.3	0.11	0.13	X	
38	10.9:	251.7:	0.19:	0.23:	2.0:	
41	6.3	150.4	0.10	0.12	2.1	
42	7.4	207.0	0.09	0.11	2.1	
44	9.6:	190.2:	0.20:	0.26:	1.9:	
46	7.9	207.1	0.05	0.06	1.9	
49	7.9	89.4	0.13	0.16	X	
52	8.5	190.6	0.03	0.04	2.1	
54	3.5	50.2	0.06	0.07	X	
55	6.5	115.9	0.17	0.21	2.5	
56	7.2	89.9	0.09	0.11	X	
58	3.9	-77.8	0.15	0.18	4.1	
60	16.2	-213.6	0.04	0.04	X	
63	9.4	31.5	0.19	0.25	2.6	
64	7.2	-216.3	0.04	0.05	2.6	
65					1.3	PS
66	5.5	-111.1	0.03	0.04	2.8	
67	7.9	-127.0	0.03	0.04	4.6: Z	
68	16.7	-388.0	0.04	0.04	2.8	
70	6.2	-82.0	0.13	0.16	X	
71	5.5	-67.4	0.06	0.07	3.6	
73	10.5	-261.7	0.04	0.05	1.9	
74	6.2	-93.9	0.07	0.09	3.6	
75	7.5	-157.5	0.05	0.06	2.7	
76	16.8	-223.1	0.03	0.03	5.0: Z	
77					2.4	PS
78	5.4	-87.5	0.19	0.24	3.4: Z	
79					1.5	PS
81	8.2	-75.8	0.04	0.05	X	
85	7.2:	-224.1	0.30	0.39:	1.2	

Table 3. Table 3 continued

JaSt	Dist kpc	z pc	R pc	M_{ion} $M_{\odot}$	E(B-V)	Comment
86	6.6	-193.0	0.18	0.23	1.9	
89	7.2	-138.3	0.15	0.19	2.1	
90	17.2:	-303.3:	0.23:	0.29:	2.1	
93	6.5:	-217.2:	0.27:	0.35:	1.9: Z	
95	7.4:	-157.7:	0.23:	0.28:	1.3	
97	5.9	-125.5	0.16	0.21	2.6	
98					2.7 Z	PS

Fig. 5. Longitude versus latitude of the new galactic bulge PNe detected in the radio. The numbers inside the symbols indicate their E(B-V) value.

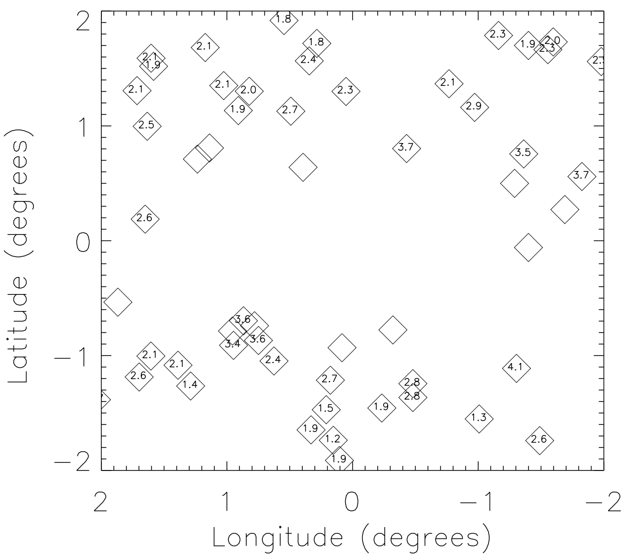

have values between 1 and 4. For the PNe detected in the radio but not in Hα the extinction is likely to be higher.

As mentioned before: some PNe were detected in Hα but not in the radio, probably due to too low surface brightness. Eight PNe were detected in the radio, but not in the Hα images, probably due to too high extinction. These PNe also show no Hα emission in their spectra. They are visible at longer wavelengths such as [S III]λ9532.

From Fig. 5 and 6 it appears indeed that the extinction increases towards the galactic center. No extinction value could be determined for objects closest to the galactic center. The distances of JaSt 54 and JaSt 58 appear to be underestimated, unless their internal extinction is very large.

7. Conclusions

We obtained the radio flux densities and diameters for 64 new galactic bulge PNe with the Australia Telescope Compact Array.

Fig. 6. Distance versus scale height of the new galactic bulge PNe detected in the radio. The numbers inside the symbols indicate their E(B-V) value.

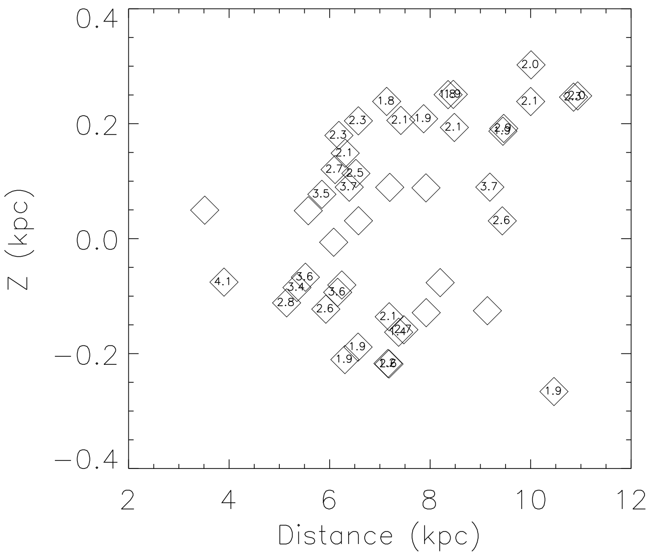

1. We have a larger ratio of larger PNe with angular diameters around 10″ and radio flux densities below 15 mJy, than in previous surveys. Our survey seems to have picked out the larger low surface brightness PNe which were missed in optical surveys to date.
2. We calculated their distances according to the method presented in Van de Steene & Zijlstra (1995). The new galactic bulge PNe are mainly located around the galactic center, and closer to it than the previously known PNe.
3. We calculated the E(B-V) extinction value based on the radio flux densities and the total Hα flux values from imaging. Only 1 PN was detected with a E(B-V) value larger than 4. Generally speaking, when E(B-V) $>$ 4.0 the galactic bulge PNe become undetectable in Hα.

References

Aaquist, A., Kwok, S., 1990, A&AS 84, 229

Acker, A., Marcout, J., Ochsenbein, F., Stenholm, Tylenda, R., 1992, Strasbourg-ESO catalogue of galactic planetary nebulae, ESO

Dopita, M.A., Vassiliadis, E., Wood, P.R., Meatheringham, S.J., Harrington, J.P., Bohlin, R.C., Ford, H.C., Stecher, T.P., Maran, S.P., 1997, ApJ 474, 188

Fomalont, E., Synthesis imaging in radio astronomy, 1989, PASP 6, ed. A. Perley, F.R. Schwab, and A. Bridle, p. 222

Kohoutek, L., 1994, Astron. Nachr. 315, 235

Pottasch, S.R., 1984, "Planetary Nebulae", D. Reidel (Dordrecht) , p.93, p.97

Pottasch, S.R., Acker a., 1989, A&A 221,123

Pottasch,S.R., 1992, A&ARv 4, 256

Sault R.J., Teuben P.J., Wright M.C.H., 1995, "A retrospective of Miriad", Astronomical Data Analysis Softwared and Systems IV, ed. R. Shaw, H.E. Payne, J.J.E. Hayes, ASP Conf. Ser., 77, 433

Van de Steene, G.C., Zijlstra, A.A., 1995, A&A, 293, 541

van Hoof, P.A.M., Van de Steene, G.C., 1999, MNRAS, 308, 623

van Hoof, P.A.M., 2000, MNRAS, 314, 99

Walsh, J.R., Jacoby, G.H., Peletier, R.F., Walton, N.A., 2000, SPIE, Discoveries and Research Prospects from 8 to 10-Meter Class Telescopes, Vol 4005, p. 131

Zijlstra, A.A., Pottasch, S.R., Bignell, C., 1989, A&AS, 79, 329

Appendix A: Contour Plots

Table 1. Optical and radio positions of the new galactic bulge PNe. The radio position is the position of the peak flux density per beam of the PN at 6 cm. Objects for which run=1 were observed in 1997, objects for which run=2 were observed in 1999

JaSt	Optical (2000.0)		Radio (2000.0)		ΔRA	ΔDEC	run	comment
	RA(h m s)	DEC (°′″)	RA(h m s)	DEC (° ′ ″)	″	″		
1	17 34 43.64	-29 47 05.03	17 34 43.60	-29 47 06.03	-0.60	1.00	2	
2	17 35 00.96	-29 22 15.72	17 35 00.96	-29 22 15.85	0.00	0.13	1	
3	17 35 22.90	-29 22 17.58	17 35 22.79	-29 22 17.08	-1.65	-0.50	1	
4	17 35 37.47	-29 13 17.67	17 35 37.39	-29 13 17.81	-1.20	0.14	1	
5	17 35 52.51	-28 58 27.95	17 35 52.44	-28 58 27.45	-1.05	-0.50	1	
7	17 38 26.69	-28 47 06.48					2	not detected
8	17 38 27.74	-28 52 01.31	17 38 27.58	-28 52 01.36	-2.40	0.05	2	
9	17 38 45.64	-29 08 59.27	17 38 45.54	-29 08 55.65	-1.50	-3.62	2	
11	17 39 00.55	-30 11 35.23	17 39 00.48	-30 11 32.23	-1.05	-3.00	2	
16	17 39 22.70	-29 41 46.08	17 39 22.64	-29 41 45.35	-0.90	-0.70	1	
17	17 39 31.32	-27 27 46.78	17 39 31.21	-27 27 47.28	-1.65	-0.50	1	
19	17 39 39.38	-27 47 22.58	17 39 39.31	-27 47 22.21	-1.05	-0.37	1	
21	17 39 52.92	-27 44 20.54					2	not detected
23	17 40 23.17	-27 49 12.04	17 40 23.08	-27 49 12.29	-1.35	0.25	1	
24	17 40 28.23	-30 13 51.30	17 40 28.19	-30 13 51.00	-0.60	-0.30	1	
26	17 40 33.52	-29 46 14.98	17 40 33.25	-29 46 12.48	-4.05	-2.50	2	
27	17 40 42.34	-28 12 31.90	17 40 42.16	-28 12 30.81	-2.7	-1.1	1	
31	17 41 27.93	-28 52 51.61	17 41 27.89	-28 52 50.61	-0.60	-1.00	1	
34	17 41 54.80	-27 03 20.33	17 41 54.69	-27 03 18.33	-1.65	-2.00	2	
36	17 42 25.20	-27 55 36.36	17 42 25.13	-27 55 36.36	-1.05	0.00	1	
37	17 42 28.60	-30 09 34.93	17 42 28.52	-30 09 32.93	-2.00	-2.00	1	
38	17 42 32.41	-27 33 15.18	17 42 32.29	-27 33 16.26	-1.80	1.08	1	
41	17 42 49.96	-27 21 19.68	17 42 49.85	-27 21 19.31	-1.65	-0.37	1	
42	17 43 17.06	-26 44 17.67	17 43 16.98	-26 44 18.25	-1.20	0.58	1	
44	17 43 23.48	-27 34 06.03	17 43 23.52	-27 34 06.55	0.60	0.52	1	
45	17 43 23.44	-27 11 16.91					2	not detected
46	17 43 30.43	-26 47 32.33	17 43 30.36	-26 47 31.83	-1.05	-0.50	1	
49	17 44 04.34	-28 15 57.86	17 44 04.23	-28 15 56.99	-1.65	-0.87	1	
52	17 44 37.30	-26 47 25.23	17 44 37.23	-26 47 25.23	-1.05	0.00	1	
54	17 45 11.06	-27 32 36.80	17 45 11.02	-27 32 36.80	-0.60	0.00	2	
55	17 45 37.36	-27 01 18.44	17 45 37.15	-27 01 18.16	-3.15	-0.28	1	
56	17 45 47.05	-27 30 42.03	17 45 46.96	-27 30 42.01	-1.35	-0.02	2	
58	17 46 52.20	-30 37 42.83	17 46 52.32	-30 37 42.33	1.80	-0.50	2	
60	17 47 53.91	-29 36 49.67	17 47 53.91	-29 36 49.67	0.00	0.00	2	
63	17 48 46.27	-27 25 37.22	17 48 46.27	-27 25 36.72	0.00	-0.50	1	
64	17 48 56.04	-31 06 41.95	17 48 56.04	-31 06 42.45	0.00	0.50	1	
65	17 49 20.02	-30 36 05.57	17 49 20.02	-30 36 05.08	0.00	0.23	1	
66	17 49 22.15	-29 59 27.02	17 49 22.11	-29 59 27.02	-0.60	0.00	2	
67	17 49 28.10	-29 20 47.56	17 49 28.02	-29 20 47.56	-1.20	0.00	2	
68	17 49 50.87	-30 03 10.47	17 49 50.83	-30 03 10.97	-0.60	0.50	2	
69	17 50 10.04	-29 19 05.14	17 50 10.11:	-29 19 08.82:	1.05	3.68	1	
70	17 50 21.07	-28 39 02.46	17 50 21.03	-28 39 01.46	-0.60	1.0	2	
71	17 50 23.32	-28 33 10.95	17 50 23.21	-28 33 10.45	-1.65	-0.50	1	
73	17 50 47.74	-29 53 16.01	17 50 47.82	-29 53 14.01	1.20	-1.99	2	
74	17 50 46.85	-28 44 35.42	17 50 46.77	-28 44 34.92	-1.20	-0.50	1	
75	17 50 48.08	-29 24 43.60	17 50 48.00	-29 24 43.18	-1.20	-0.42	1	
76	17 50 56.47	-28 31 24.63	17 50 56.33	-28 31 24.13	-2.10	-0.50	2	
77	17 51 11.65	-28 56 27.20	17 51 11.58	-28 56 27.20	-1.20	0.00	1	
78	17 51 24.68	-28 35 40.34	17 51 24.79	-28 35 39.44	1.65	-0.90	1	
79	17 51 53.63	-29 30 53.41	17 51 53.55	-29 30 53.41	-1.20	0.00	1	
80	17 51 55.54	-27 48 02.46					1	not detected
81	17 52 04.35	-27 36 39.28	17 52 04.28	-27 36 38.28	-1.05	1.00	1	
83	17 52 45.17	-29 51 05.21	17 52 45.17	-29 51 03.30	0.00	-1.91	1	
85	17 52 49.05	-29 41 54.92	17 52 48.97	-29 41 55.92	-1.20	1.0	2	

Table 1. Table 1 continued

JaSt	Optical (2000.0)		Radio (2000.0)		ΔRA	ΔDEC	run	comment
	RA(h m s)	DEC (° ′ ″)	RA(h m s)	DEC (° ′ ″)	″	″		
86	17 52 52.20	-29 30 00.07	17 52 52.16	-29 30 01.08	-0.60	1.08	1	
88	17 53 00.89	-29 05 44.08					2	not detected
89	17 53 06.67	-28 18 07.91	17 53 06.79	-28 18 10.47	1.80	2.56	1	
90	17 53 17.77	-28 04 33.20	17 53 17.73	-28 04 32.67	-0.60	-0.53	2	
92	17 53 19.81	-28 27 14.67					2	not detected
93	17 53 24.14	-29 49 48.45	17 53 24.05:	-29 49 51.15:	-1.35	2.70	1	
95	17 53 35.38	-28 28 51.02	17 53 35.51	-28 28 51.96	1.95	0.94	1	
96	17 53 57.16	-29 20 14.97					2	not detected
97	17 54 13.36	-28 05 16.82	17 54 13.28	-28 05 16.82	-1.20	0.00	1	
98	17 55 46.39	-27 53 38.91	17 55 46.28	-27 53 38.41	-1.65	-0.50	1	

Table 2. Radio flux densities at 6 and 3 cm, and angular sizes are presented. The name of the PN is listed in the first column. The second to sixth columns give the peak flux density per beam, the total radio flux density, the error estimate, and the rms in the map respectively. Columns six to nine list the same quantities at 3 cm. The tenth column gives the deconvolved FWHM in arcsec ($\Delta\delta$ x $\Delta\alpha$). The eleventh column gives the FWHM of the beam major and minor axis in arcsec ($\Delta\delta$ x $\Delta\alpha$). The thirteenth column gives the equivalent FWHM diameter. The fourteenth column indicates whether the diameter FWHM is the deconvolved FWHM determined after fitting a Gaussian model (G) or after measuring the size from the contour plot (C). All diameters were determined at 6 cm unless otherwise mentioned. The last column gives an estimate of the full equivalent diameter as explained in the text. PS stands for Point Source. Values which are very uncertain are marked with a colon.

Name JaSt	6cm Peak mJy/ beam	Flux mJy	error mJy	noise mJy/ beam	3cm Peak mJy/ beam	Flux mJy	error mJy	noise mJy/ beam	size $\Delta\delta$ x $\Delta\alpha$ $''$ x $''$	beam maj x min $''$ x $''$	FWHM diam $''$	method	θ diam $''$
1	0.85	1.6	0.2	0.10	0.47	1.4	0.6	0.12	4.5 x 2.6	4.3 x 1.9	3.4	G	5.5
2	1.8	4.3	0.5	0.22	0.82	4.2	1.4	0.12	5.0 x 4.0	4.7 x 1.8	4.5	C	6.3
3	4.0	12.4	1.2	0.17	1.6	10.0	1.0	0.13	5.8 x 4.4	4.8 x 2.0	5.1	C	9.2
4	1.2	4.1	0.4	0.20	0.65	3.5	1.2	0.15	7.7 x 7.1	4.7 x 1.8	7.4	C	11.2
5	4.0	11.3	1.1	0.15	1.8	10.5	1.0	0.15	6.2 x 5.1	4.9 x 2.0	5.6	C	8.4
8	1.2	3.8	0.4	0.08	0.5	2.6	0.6	0.04	3.6 x 5.8	4.4 x 1.9	4.6	C	7.2
9	0.96	4.0	0.4	0.08	0.38	2.5	0.8	0.08	5.6 x 6.2	4.7 x 1.8	5.9	C	8.1
11	0.76	3.3	0.3	0.07	0.41	>2.0		0.12	6.9 x 5.9	4.6 x 1.8	6.4	C	10.9
16	13.6	27.0	2.8	0.27	7.2	24.7	2.5	0.30	3.4 x 2.4	4.8 x 2.0	2.9	G	4.8
17	2.5	9.4	1.0	0.15	1.2	8.2	0.9	0.13	5.4 x 5.3	5.7 x 1.8	5.3	C	7.9
19	2.1	6.8	0.8	0.29	1.0	5.5	0.6	0.14	3.6 x 3.7	5.3 x 1.6	3.6	C	6.8
23	3.3	3.7	0.4	0.25	2.6	3.9	0.4	0.21	PS	3.1 x 1.1	<1.8	G$_{3cm}$	
24	6.3	16.0	1.7	0.27	2.7	14.1	1.4	0.23	4.8 x 2.7	4.9 x 1.7	3.6	G	5.8
26	2.4	14.1	1.4	0.09	1.0	9.0	0.9	0.08	9.4 x 9.3	5.1 x 1.7	8.5	C	11.1
27	0.8	2.5	0.3	0.14	0.5			0.15	9.9 x 5.3	5.3 x 1.7	8.2	C	8.7
31	3.3	11.5	1.2	0.22	2.4	>3.0		0.61	5.0 x 5.1	5.1 x 1.7	5.0	C	9.0
34	0.58	1.7	0.2	0.07	0.34	>1.5		0.09	3.2 x 6.0	5.1 x 1.7	4.4	C	7.1
36	18.6	31.1	3.1	0.33	11.7	31.1	3.1	0.35	2.6 x 1.9	3.1 x 1.1	2.2	G$_{3cm}$	3.6
37	5.2	16.0	1.7	0.70	2.5	>5.5		0.35	5.7 x 3.8	4.6 x 1.5	4.6	C	7.4
38	1.2	3.0	0.6	0.28	0.9	2.0	0.7	0.15	6.8 x 2.2	5.3 x 1.7	3.9	C	7.0
41	8.0	16.7	1.7	0.20	4.6	17.6	1.8	0.18	3.4 x 3.2	5.6 x 1.8	3.3	C	6.3
42	5.6	12.9	1.3	0.21	3.3	15.5	1.6	0.26	4.0 x 2.5	5.5 x 1.6	3.1	G	5.0
44	1.3	3.8	1.0	0.27	0.9	>1.8		0.27	12.2: x 6.0:	5.4 x 1.6	8.6:	C	8.6:
46	14.6	20.8	2.1	0.40	12.3	20.5	2.1	0.30	2.0 x 1.1	3.3 x 1.1	1.5	G	2.5
49	3.1	8.2	0.9	0.27	2.1	10.8	1.1	0.21	4.6 x 3.6	5.2 x 1.6	4.0	C	6.6
52	20.8	24.0	2.4	0.34	16.9	22.8	2.3	0.40	2.5 x 0.4	3.3 x 1.1	1.0	G$_{3cm}$	1.7
54	21.9	82.3	8.2	0.08	7.5	75.2	7.5	0.09	4.7 x 4.3	5.1 x 1.8	4.5	G	7.2
55	2.0	9.2	0.9	0.19	0.9	10.0	2.0	0.17	5.5 x 6.4	5.4 x 1.6	6.0	C	10.7
56	5.8	14.1	1.4	0.09	2.4	12.2	1.2	0.07	3.8 x 2.7	2.8 x .95	3.2	G$_{3cm}$	5.0
58	3.5	29.5	2.9	0.06	1.3	21.3	2.1	0.07	8.9 x 8.0	4.6 x 1.7	8.4	C	15.5
60	6.1	6.5	0.7	0.06	7.0	7.9	0.8	0.07	.85 x .28	2.6 x 1.0	0.5	G$_{3cm}$	0.9
63	1.1	3.9	0.4	0.11	0.7	3.6	1.2	0.13	6.1 x 6.0	5.5 x 1.8	6.0	C	8.4
64	23.8	28.3	2.9	0.42	15.8	25.6	2.6	0.58	2.0 x 0.7	5.0 x 1.9	1.4	G	2.4
65	3.3	3.4	0.4	0.23	6.3	6.6	0.7	0.30	PS	2.7 x 1.0	< 1.6	G$_{3cm}$	
66	45.9	65.3	6.5	0.15	26.0	60.9	6.1	0.10	2.0 x 1.5	2.6 x 1.00	1.7	G$_{3cm}$	2.8
67	24.6	27.8	2.8	0.08	17.7	26.0	2.6	0.10	1.3 x .9	2.5 x 1.0	1.1	G $_{3cm}$	1.8
68	5.4	5.9	0.6	0.06	7.7	8.8	0.9	0.10	.8 x .3	2.5 x 1.0	1.5	G$_{3cm}$	0.9
69	0.9	>2.0		0.26	0.5	>2.0		0.15		4.9 x 1.7			
70	4.0	13.0	1.3	0.11	1.9	11.5	1.2	0.06	4.3 x 5.3	4.6 x 1.7	4.8	C	8.5
71	20.2	34.0	3.5	0.50	10.0	36.0	3.6	0.55	4.6 x 1.6	5.4 x 1.9	2.7	G	4.5
73	11.7	13.7	1.4	0.09	9.4	13.0	1.3	0.11	1.3 x .7	2.6 x 1.0	0.95	G$_{3cm}$	1.6
74	12.7	22.7	2.3	0.28	6.1	22.2	2.2	0.25	4.5 x 2.2	3.3 x 1.0	3.1	G$_{3cm}$	4.9
75	16.8	22.5	2.3	0.53	11.0	19.0	2.0	0.55	3.0 x 0.9	5.0 x 1.6	1.6	G	2.7
76	5.4	7.4	0.7	0.07	2.5	6.7	0.7	0.08	3.9 x 1.8	2.4 x 1.0	2.6	G$_{3cm}$	4.7
77	39.4	49.0	5.0	0.85	34.0	51.2	5.1	0.98	PS	3.1 x 1.1	<1.5	G$_{3cm}$	
78	1.5	12.3	1.2	0.18	0.9	9.0	2.3	0.15	12.0 x 9.0	5.1 x 1.6	10.4	C	14.6
79	4.1	4.1	0.4	0.14	6.7	7.0	0.7	0.23	PS	2.7 x 1.2	<1.5	G$_{3cm}$	

Table 2. Table 2 continued

Name	6cm				3cm				size	beam	FWHM	method	θ
JaSt	Peak	Flux	error	noise	Peak	Flux	error	noise	$\Delta\delta$ x $\Delta\alpha$	maj x min	diam		
	mJy/	mJy	mJy	mJy/	mJy/	mJy	mJy	mJy/	$''$ x $''$	$''$ x $''$	$''$		
	beam				beam	beam			beam				
81	17.8	20.8	2.0	0.25	14.1	20.8	2.1	0.29	1.8 x 0.7	5.1 x 2.0	1.3	G	2.2
83	1.7	5.0:	2.5	0.40	0.6	>0.6		0.16	5.3: x 5.7:	4.5 x 1.8	>5.5:	C	>6.3
85	0.6	4.4	1.2	0.09					13.1: x 13.1:	4.2 x 1.9	13.1:	C	17.5:
86	1.7	8.5	0.9	0.17	0.9	>2.5		0.17	7.5 x 7.7	4.7 x 1.8	7.6	C	11.4
89	1.8	8.5	0.9	0.27	0.8	>2.0		0.19	9.5 x 5.5	4.8 x 1.7	7.2	C	8.6
90	0.51	1.0	0.2	0.07				0.13	4.5 x 2.5	4.4 x 1.9	3.4	G	5.5
93	0.8	6.3	0.9	0.15	0.6	>2.1		0.13	20.2 x 8.0	4.8 x 2.0	12.7:	C	17.8:
95	1.1	5.5	1.0	0.25	0.7	4.5:	1.5	0.18	14.6 x 7.5	4.8 x 1.8	10.5	C	12.6
97	2.7	11.5	1.2	0.16	1.2	11.8	1.2	0.18	8.0 x 5.9	5.2 x 1.9	6.8	C	11.4
98	21.0	21.8	2.2	0.38	20.3	24.0	2.4	0.46	PS	2.9 x 1.1	<1.5	G_{3cm}	